RESEARCH ARTICLE
ATMOSPHERIC PHYSICS

Earth and Planetary Physics
3: 147–156, 2019
doi: 10.26464/epp2019018

Role of tropical cyclones over the western North Pacific in the East Asian summer monsoon system

Xian Chen[1], Zhong Zhong[3,4*], YiJia Hu[3], Shi Zhong[2], Wei Lu[3], and Jing Jiang[4]

[1]China Aerodynamics Research and Development Center, Mianyang Sichuan 621000, China ;

[2]State Key Laboratory of Hydrology-Water Resources and Hydraulic Engineering, Hohai University, Nanjing 210098, China ;

[3]College of Meteorology and Oceanography, National University of Defense Technology, Nanjing 211101, China ;

[4]Jiangsu Collaborative Innovation Center for Climate Change, Nanjing University, Nanjing 210093, China

Abstract: Precipitation observations collected at weather stations in eastern China, the NCEP/NCAR reanalysis data, the tropical cyclone (TC) Best Track Dataset, and a sensitivity numerical experiment were used in the present study to investigate the role in the East Asian summer monsoon (EASM) system played by frequent TC activities over the western North Pacific (WNP). Results indicated that, in active TC years, the EASM is stronger and the southerly winds in the lower troposphere advance farther north and reach higher latitudes. Meanwhile, the monsoon rain belt remains in the lower and middle reaches of the Yangtze River valley for a relatively short period, leading to less precipitation there. Both the western Pacific subtropical high and the South Asian high weaken with the northward shift of the ridgelines for both high-pressure systems as well as the East Asian subtropical upper-level jet. Therefore, the impacts of frequent TC activities over the WNP on each individual component of the EASM are in phase with those of the stronger EASM itself, amplifying features of the already strengthened EASM.

Keywords: East Asian summer monsoon; tropical cyclone; western North Pacific

Citation: Chen, X., Zhong, Z., Hu, Y. J., Zhong, S., Lu, W., and Jiang, J. (2019). Role of tropical cyclones over the western North Pacific in the East Asian summer monsoon system. *Earth Planet. Phys.*, *3*(2), 147–156. http://doi.org/10.26464/epp2019018

1. Introduction

The East Asian summer monsoon (EASM) is the principal large-scale circulation system that exhibits distinct interannual variability and controls the weather and climate in East Asia (EA) (Lu RY 2004; Huang RH et al., 2007). The land–sea thermal contrast between the EA land and the western North Pacific (WNP) is one of the major reasons for the formation of the EASM, where El Niño–Southern Oscillation cycles, snow cover changes in the Tibetan Plateau, and soil moisture anomalies in EA all contribute to changes in the temperature difference between land and ocean and subsequently affect the formation and evolution of the EASM (Wang ZQ et al. 2014; Liu BQ et al., 2015). In addition, the atmospheric teleconnection patterns in the summer over EA have great impacts on the EASM, and convective activities in the tropical ocean can trigger meridionally propagating Rossby wave trains, which affect the summer monsoon circulation and monsoon onset in EA (Kawamura and Ogasawara, 2006; Zhong Z et al., 2015). Moreover, warm local sea surface temperature (SST) anomalies have been found to heat the atmosphere directly above and affect the atmospheric circulation. For example, Ren XJ et al. (2013) proposed that warm SST anomalies in the WNP could lead to westward expansion and intensification of the western Pacific subtropical high (WPSH), resulting in persistent precipitation in the lower and middle reaches of the Yangtze River valley (LMYRV). Warm SST anomalies in the tropical Indian Ocean can heat the tropospheric atmosphere, leading to an intensification and southward shift of the South Asian High (SAH) (Huang G et al., 2011) and a southward shift of the East Asian subtropical upper-level jet (EASJ) (Qu X and Huang G, 2012).

The WNP is the most active tropical cyclone (TC) basin worldwide, with more than 30% of global TCs forming in this region (Matsuura et al., 2003). Previous studies have shown that the WNP TCs are significantly correlated with the EASM (Choi et al., 2016). However, most of the available studies have focused only on the effect of modulating the large-scale EASM on TC activities. In fact, a TC represents a circulation system with a strong vortex, which makes great contributions to vorticity anomalies in the monsoon trough region in the summer and autumn (Hsu et al., 2008; Ha Y et al., 2013). During the westward and northward movement of TCs, large amounts of atmospheric heat, momentum, and moisture are transported to EA, leading to changes in the WPSH and precipitation (Jansen and Ferrari 2009; Ha et al. 2013). However, the role that TC activities over the WNP play in interannual variability of the EASM system is not mentioned in the literature. In the present study, precipitation observations collected at weather stations in eastern China, the NCEP/NCAR reanalysis, and the TC Best Track Dataset are used to compare features of the EASM system in act-

Correspondence to: Z. Zhong, zhong_zhong@yeah.net
Received 24 JAN 2019; Accepted 20 MAR 2019.
Accepted article online 25 MAR 2019.

ive and inactive TC summers. Frequent WNP TC activities are found to induce further intensification of the already strong EASM features, and the possible mechanisms behind this are investigated.

This article is organized as follows. In Section 2, we describe the data, monsoon indexes, and experimental design of the present study. Observational analyses and possible mechanisms for the role that TC activities play in the EASM system are presented in Sections 3 and 4, respectively. Finally, conclusions and a discussion are given in Section 5.

2. Data, Indexes, and Numerical Experimental Design

2.1 Data

The TC Best Track Dataset from the Regional Specialized Meteorological Center Tokyo Typhoon Center for the summer (June–August) of 1961–2010 was used in this study (JMA, 2012). This dataset includes the TC name, TC position in latitude and longitude, center pressure, and maximum sustained wind at 6-h intervals. Only those TCs reaching tropical storm intensity (maximum sustained wind speed $\geq$17.2 m·s^{-1}) were selected for this study. Daily precipitation records at 986 stations in the area between 110°E and 120°E were provided by the National Meteorological Information Center of the China Meteorological Administration. Atmospheric winds and geopotential height were extracted from the NCEP/NCAR reanalysis at 6-h intervals at 2.5° × 2.5° resolution (Kalnay et al., 1996), whereas the initial and lateral boundary conditions for numerical experiments were from the NCEP/NCAR reanalysis at 6-h intervals at 1° × 1° resolution (https://doi.org/10.5065/D6M043C6).

2.2 Definitions of Indices

To describe TC activities over the WNP, the TC track density is defined as the TC count that appears in 5° × 5° grids during the summertime. Following the approach suggested by Wang B et al. (2004), the monsoon index is defined in the present study as the area-averaged zonal wind at 850 hPa within a key region (5°N–15°N, 110°E–120°E). For the WPSH, the mean position of the ridgeline is represented by the average latitude of the ridgelines within 100°E–150°E with a geopotential height greater than 585 dagpm at 500 hPa. The ridgeline at grid points was determined based on zonal wind speed $u = 0$ and $\partial u/\partial y > 0$ in the northern hemisphere (Liu YM and Wu GX, 2004). The westward extension index is represented by 500 hPa geopotential height anomalies in the key region (110°E–130°E, 20°N–30°N). The intensity index is calculated by the accumulative value of differences between 585 dagpm and the geopotential height at 500 hPa for grid points within 100°E–150°E, 10°N–50°N where the geopotential height is greater than 585 dagpm. Similar to that for WPSH, the mean position of the SAH ridgeline is represented by the averaged latitude of all ridgelines at grid points within 90°E–140°E with a geopotential height greater than 1,246 dagpm at 200 hPa. The eastward extension index is represented by geopotential height anomalies at 200 hPa within the key region 22.5°N–32.5°N, 100°E–120°E (Ren XJ et al., 2015). The intensity index is defined as the accumulative value of differences between 1,247 dagpm and 200 hPa geopotential height for grid points within 90°E–140°E, 10°N–50°N where the geopotential height is greater than 1,247 dagpm (Zhang PF et al., 2016).

2.3 Composite Analysis

Figure 1 shows the interannual variation of summertime TC counts over the WNP in JMA. Here, we define the TC active years (hereafter AY) as the 10 years with the most TC counts, which are indicated by an × in Figure 1. We then define the TC inactive years (hereafter IY) as the 10 years with the least TCs, which are represented by a triangle (Δ) in Figure 1. As shown in Figure 1, the AY are identified as 1962, 1964, 1965, 1966, 1967, 1971, 1989, 1992, 1994, and 2004, and the IY include 1969, 1975, 1979, 1980, 1983, 1995, 1998, 2007, 2008, and 2010. Changes of the composite atmospheric circulation and precipitation in the AY and IY are investigated to represent the impacts of WNP TC activities.

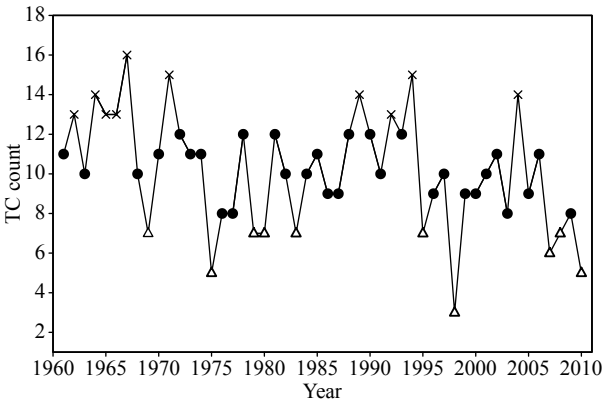

Figure 1. Interannual variation of summertime TC counts over the WNP. The letter × and triangle (Δ) represent the AY and IY, respectively.

2.4 Experimental Design

Two ensemble simulations were performed in this study to separate the impact of WNP TC activities on the EASM system. In the control runs (hereafter CR), the Weather Research and Forecasting (WRF) model, version 3.4.1 was used to simulate WNP TC activities and the corresponding large-scale background circulation from year 2000 to 2009. The WRF is continuously integrated from 00:00 UTC 01 June to 00:00 UTC 01 September every year. The center of the model domain is located at 27°N, 135°E, with a grid spacing of 30 km covering 352 × 350 points. The model top is 50 hPa with 35 vertical levels. The lateral boundary forcing is updated at 6-h intervals, and the integration time step is 30 s. The time interval for the model output is 6 h. Important physical schemes include the WRF single-moment 3-class microphysics scheme, the Kain-Fritsch (New Eta) cumulus parameterization scheme, the Rapid Radiative Transfer Model long-wave radiation scheme, the Dudhia short-wave radiation scheme, the Mellor-Yamada-Janjic planetary boundary scheme, the Unified Noah land surface scheme, and the Monin-Obukhov similarity theory for surface layer physics. Detailed description of the WRF dynamics and physics can be found in Skamarock et al. (2008).

The sensitivity experiment (hereafter SR) was conducted by use of the "modeling surgery" methodology, which adds a TC suppres-

sion module to the WRF. The TC suppression module suppresses the generation and development of WNP TCs and is worked for every integration time step. The workflow for the TC suppression module is as follows: first, the relative vorticity is calculated over the WNP between 0°N and 30°N near 850 hPa; second, these grids are searched for where the relative vorticity is larger than 5×10^{-5} s^{-1}; and third, u and v at the grids are replaced by the 9-point smoothed u^* and v^*, as represented in equations (1) and (2):

$$u^*(i,j) = \frac{1}{9}\sum_{a=i-1}^{i+1}\sum_{b=j-1}^{j+1} u(a,b), \tag{1}$$

$$v^*(i,j) = \frac{1}{9}\sum_{a=i-1}^{i+1}\sum_{b=j-1}^{j+1} v(a,b), \tag{2}$$

where u and v are the zonal wind and meridional wind, respectively, in the projection plane of the WRF model. As proposed in previous studies, choosing the criterion for the relative vorticity over 5×10^{-5} s^{-1} near 850 hPa can effectively distinguish TCs from other low-intensity vortices for the ~30 km grid distance in this work (Su ZZ et al., 2010; Kim D et al., 2015). Equations (1) and (2) are moving average methods that can be used to reduce the difference between two grids. As a consequence, the relative vorticity in those grids will decline, and the genesis and development of WNP TCs are suppressed because of the low level of relative vorticity (Fu B et al., 2012; Ge XY et al., 2013). Other than that, all other options in the SR were the same as in the CR, and no TC circulation occurred in the model domain when the TC suppression module was employed for the SR.

3. Composite Analysis Results

Statistical analysis indicates that in total, 140 TCs formed in the AY, whereas only 61 TCs formed in the IY, less than half the number in the AY. Most of these TCs moved northwestward and northward after their formation, affecting the middle and high latitudes. In the AY, 37 TCs in total made landfall in the continent of Asia, and 55 TCs reached north of 35°N, whereas in the IY, the corresponding numbers were only 19 and 15, respectively. Figure 2 displays the TC track densities averaged over 5° × 5° grids in the AY, the IY, and their differences. In both the AY and IY, the maximum WNP TC track density was located at the Bashi Channel and the ocean to its east, but both the area of TC activity and the TC track density were much larger in the AY than the IY. The largest TC track density was 15 per year in the AY, but this value was only 9 per year in the IY (Figure 2a, 2b). Within the area of TC activity, the TC track density in the AY was always larger than that in the IY; therefore, the differences between the AY and the IY were always positive. The largest difference of 7 per year was located over the ocean to the east of the Bashi Channel at approximately 135°E (Figure 2c). Large differences in TC numbers appeared to exist between the AY and IY, although the features of TC activity were basically the same.

Figure 3 shows 10-year mean daily evolutions of the EASM index as defined by Wang B et al. (2004) in the AY and IY in summer. As shown in Figure 3, the EASM index in the AY was almost larger than that in the IY, indicating that the EASM was stronger in the AY. Next, the features of the EASM components, including the monsoon flow at a lower troposphere and WPSH, SAH, and EASJ in the AY and IY, were further investigated to reveal the impacts of TC activities on the EASM system.

Figure 4 presents the latitude–time cross sections of meridional winds averaged over 110°E–120°E at 850 hPa in the summer. This figure clearly shows that the maximum southerly wind in both the AY and IY was around 7 $m \cdot s^{-1}$; however, southerly winds could reach about 50°N in the AY (Figure 4a), and they could reach only about 45°N in the IY (Figure 4b). In midsummer of the AY, southerly winds greater than 3 $m \cdot s^{-1}$ could expand to the north of 30°N and reach about 40°N in middle and late July; in the IY, however, southerly winds greater than 3 $m \cdot s^{-1}$ could reach only a northernmost latitude of around 30°N, which was almost 10° to the south compared with that in the AY. The difference between the AY and IY showed that southerly winds to the north of 30°N were basically stronger in the AY than in the IY (Figure 4c). Overall, the southerly winds in the summer were stronger in the AY than in the IY and could reach higher latitudes.

The EASM rain belt is usually located at the convergence area of southerly and northerly winds in the lower troposphere, which advances northward following the northward expansion of southerly winds after the onset of the EASM (Tao SY and Chen LX, 1987).

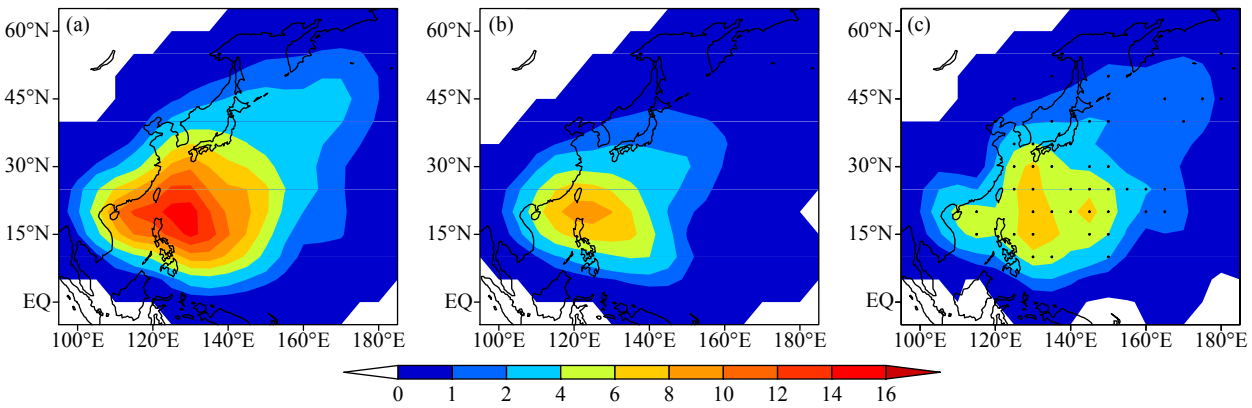

Figure 2. Distributions of summertime mean TC track density over the WNP in a 5° × 5°grid box for (a) the AY, (b) the IY, and (c) differences between the AY and IY. The dotted areas in (c) represent significance at the 95% confidence level or higher.

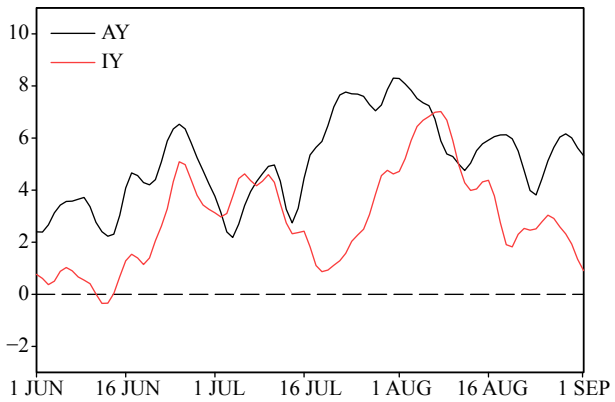

Figure 3. Composite temporal evolution of the daily EASM index for the AY (black) and the IY (red).

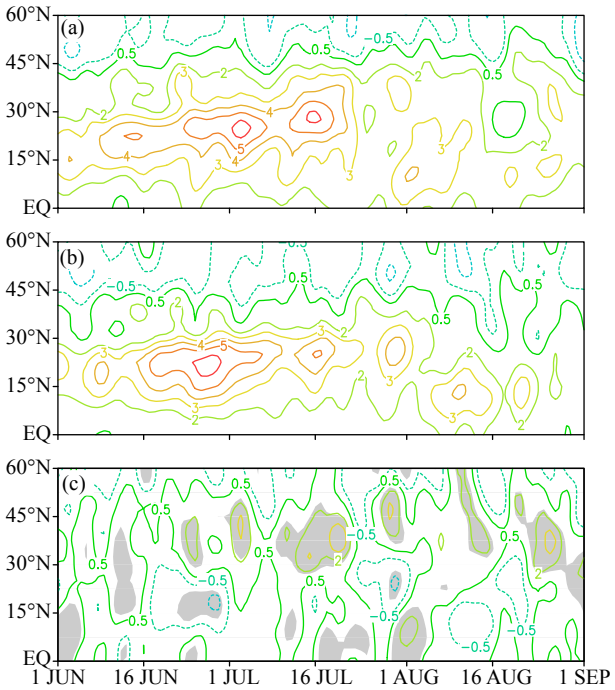

Figure 4. Latitude–time cross sections of daily meridional winds (unit: m·s^{-1}) at 850 hPa averaged along 110°E–120°E for (a) the AY, (b) the IY, and (c) differences between the AY and IY. The gray areas in (c) represent significance at the 95% confidence level or higher.

Figure 5 presents the latitude–time cross sections of the summertime average precipitation rate over 110°E–120°E in the AY and IY. Summertime precipitation can be seen to move gradually northward following the advance of monsoons in both the AY and IY (Figure 5a, 5b). Before mid-June, large areas of precipitation were located to the south of 30°N; however, from late June, the rain belt moved to the north of 30°N and remained there until mid-July. This is the so-called Meiyu period in China. Specifically, in the AY, the rain belt started to move northward by around June 20; it then rapidly advanced northward and reached around 40°N by about July 10. Beginning from mid-August, the rain belt gradually retreated southward with decreasing precipitation (Figure 5a). In contrast, in the IY, the rain belt started to move northward about

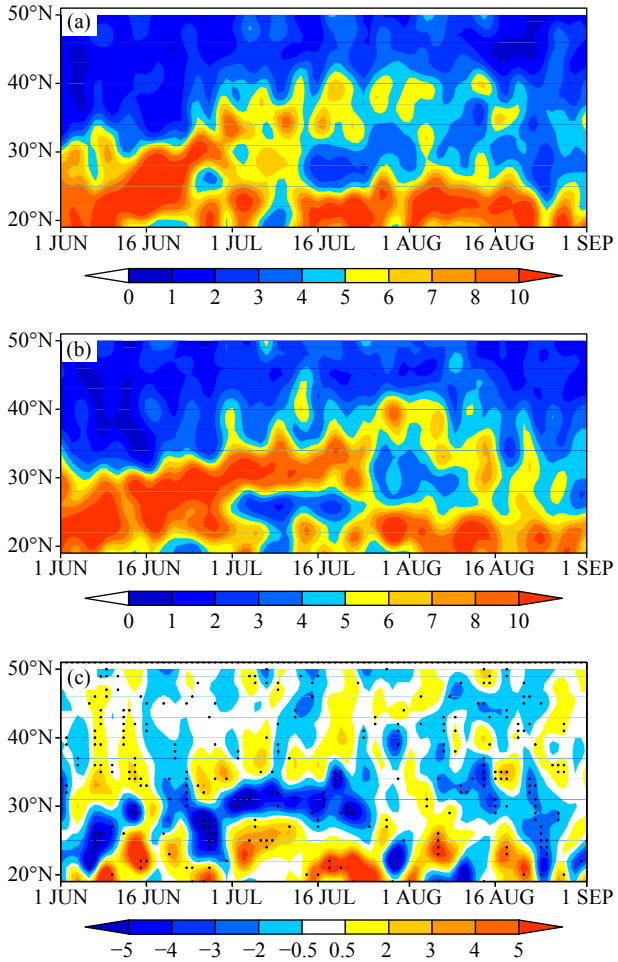

Figure 5. Latitude–time cross sections of precipitation rate (unit: mm·day^{-1}) averaged along 110°E–120°E for (a) the AY, (b) the IY, and (c) differences between the AY and IY. The dotted areas in (c) represent significance at the 95% confidence level or higher.

one week later than for the AY and reached 31°N by about July 5. The rain belt then advanced northward again and reached 39°N in late July. Precipitation decreased thereafter, and the rain belt rapidly retreated southward (Figure 5b). The differences in precipitation evolution between the AY and IY showed negative centers located near 25°N before mid-June and at around 30°N from late June to early July, whereas a positive precipitation difference occurred to the south and north (Figure 5c). These results indicate that frequent WNP TC activities can affect the evolution of the EASM rain belt and result in positive EASM precipitation anomalies in South China and significant negative precipitation anomalies in the LMYRV during the Meiyu period, as suggested by Zhu Z et al. (2017). In addition, precipitation in the midsummer increased to the north of the Yangtze River and Huaihe River basin in the AY.

The composite temporal evolutions of the summertime daily ridgeline position, westward extension index, and intensity index of the WPSH in the AY and IY are shown in Figure 6. The WPSH ridgeline is shown to advance steadily northward from June in both the AY and IY, and the ridgeline reached its northernmost position of 33°N in late July in the AY before it began to retreat

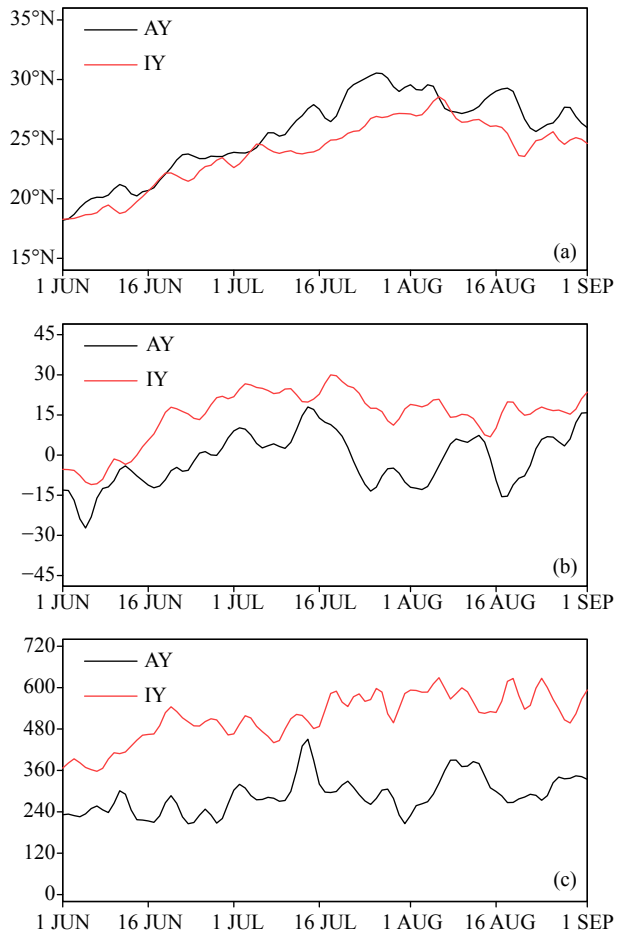

Figure 6. Composite temporal evolutions of (a) the daily mean latitude of the WPSH ridgeline averaged along 100°E–150°E, (b) the westward extension index of the WPSH, and (c) the intensity index of the WPSH for the AY (black) and the IY (red) at 500 hPa.

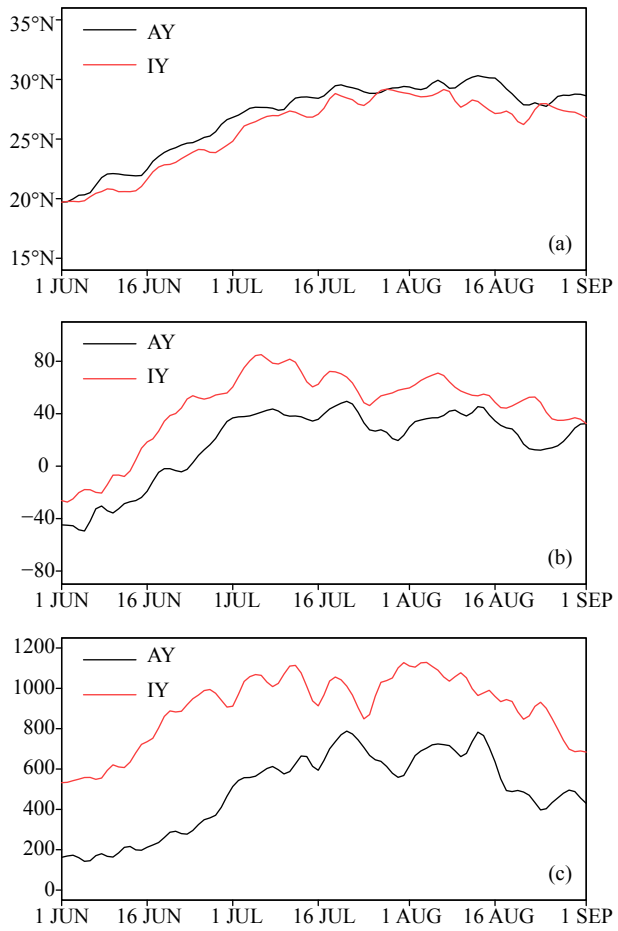

Figure 7. Composite temporal evolutions of (a) the daily mean latitude of the SAH ridgeline averaged along 90°E–140°E, (b) the eastward extension index of the SAH, and (c) the intensity index of the SAH for the AY (black) and the IY (red) at 200 hPa.

southward. However, it reached its northernmost position of 30°N only in early August and then rapidly retreated southward in the IY (Figure 6a). Moreover, the WPSH ridgeline in summer of the AY was almost always located to the north of that in the IY, and the WPSH extended farther westward with stronger intensity in the IY than in the AY (Figure 6b, 6c). These results suggest that the WNP TC activities are closely related to spatial and temporal variations of the WPSH.

Figure 7 shows temporal variations in the summertime daily ridgeline position, eastward extension index, and intensity index of the SAH in the AY and IY, respectively. As illustrated in Figure 7a, the SAH ridgeline also steadily advanced northward in the summer for both the AY and IY, similar to the temporal evolution of the WPSH ridgeline. However, the ridgeline in the AY was almost always located farther north compared with that in the IY. Moreover, the SAH extended farther eastward with a stronger intensity in the IY than in the AY (Figure 7b, 7c). Therefore, the WNP TC activities were also associated with both the spatial distribution and temporal evolution of the SAH in the upper troposphere.

To further reveal the different impacts of summertime WNP TC activities on the high-pressure systems in the middle and upper troposphere, we averaged the 1,248 dagpm contour at 200 hPa and the 586 dagpm contour at 500 hPa over June–August in the AY and IY. Figure 8 shows the mean scopes of the SAH and WPSH in EA, respectively, and illustrates that, despite the intensities of the SAH and WPSH being weaker, the ridgelines of both the SAH and WPSH were located farther north in the AY than in the IY, especially that of the WPSH. In addition, the easternmost position of the SAH was located at around 125°E and 144°E in the AY and IY, respectively, with a difference of about 19 longitudinal degrees, whereas the characteristic contour of the WPSH was located over the ocean to the east of 125°E in the AY, but it extended westward and reached South China and the Indochina Peninsula in the IY, suggesting that the SAH and WPSH kept moving toward (away from) each other is associated with TC activities. These features associated with TC activities are similar to the seasonal variations of WPSH and SAH (Yang J et al., 2014).

The EASJ, an important component of the EASM system, is located to the north of the SAH in the upper troposphere and lower stratosphere (Liu J et al., 2010; Lu RY et al., 2011). Changes in the EASJ have important influences on cold air activities, mid-latitude cyclone movements, and the distribution of precipitation (Lu RY, 2004; Sampe and Xie SP, 2010; Liao ZJ and Zhang YC, 2013). Daily evolutions of the summertime EASJ axis averaged over

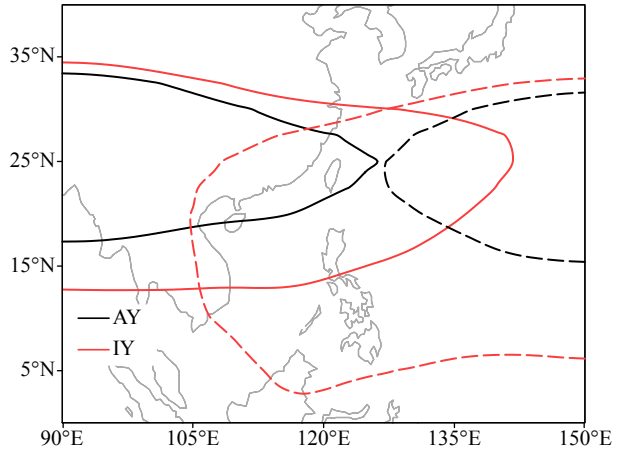

Figure 8. Contours of 1,248 dagpm at 200 hPa (solid) and 586 dagpm at 500 hPa (dashed) averaged from June to August for the AY (black) and the IY (red).

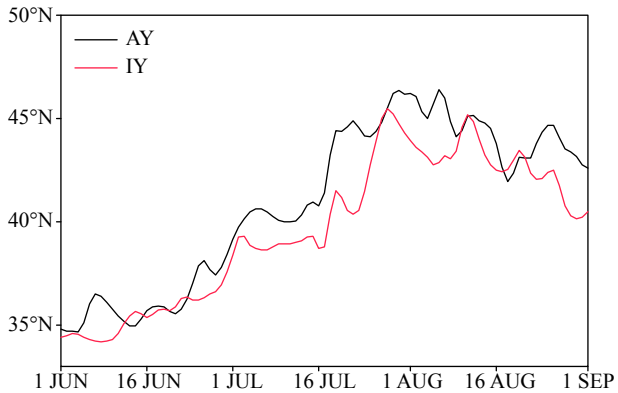

Figure 9. Composite temporal evolutions of the daily position of the EASJ axis averaged along 100°E–140°E for the AY (black) and the IY (red).

100°E–140°E in the AY and IY are displayed in Figure 9. This figure shows that the EASJ axis gradually moved northward in both the AY and IY after mid-June, whereas the axis in the AY was located farther north compared with that in the IY. In late July, the EASJ axis reached its northernmost position of 46.5°N (45.5°N) in the AY (in the IY). From early August, the axis started a steady retreat southward. It has been proposed that the northward displacement of the summertime EASJ is related to frequent TC activities over the WNP because the summertime WNP TC activities can lead to changes in the meridional temperature gradient in the EA–WNP region (Chen X et al., 2017; Hu CD et al., 2018). Results of the present study suggest that TC activities are also related to temporal evolution of the EASJ in the summer.

4. Impact Mechanism

Previous studies have indicated that the WNP TC activities can trigger quasi-stationary Rossby waves and northward-propagating Pacific–Japan teleconnection pattern wave trains, which subsequently affect atmospheric circulation at the middle and high latitudes (Kawamura and Ogasawara 2006; Chen X et al., 2017). Moreover, frequent WNP TC activities in the summer can directly affect large-scale circulation through thermodynamic processes over the EA–WNP region (Sun Y et al., 2010; Chen X et al., 2017). In this section, we discuss the possible cause of WNP TC activities on the EASM system.

Figure 10 shows the composite differences in mean wind field and geopotential height between the AY and IY at 850 hPa. The difference in circulation between the AY and IY exhibits a cyclonic circulation belt to the south of 25°N, with the center located to the east of the Bashi Channel, and an anticyclonic circulation belt to the north of 25°N, with the center located over the ocean to the east of Japan (Figure 10). Such a circulation difference pattern is somewhat like the Pacific–Japan pattern (Lu, 2004). The abnormal quasi-zonal westerlies between the AY and IY cover the region from the equator to about 15°N, suggesting that the lower troposphere westerlies in the tropics are stronger in the AY than in the IY. Additionally, abnormal southerlies appear to the north of the Yangtze River and northern China.

The height–latitude cross sections of differences in mean geopotential height and vertical velocity between the AY and IY averaged from June to August and at 110°E–150°E are shown in Figure 11. This figure shows that the geopotential differences are negative to the south of 35°N over the entire troposphere and positive to the north of 35°N in the middle and upper troposphere (Figure 11a). Consequently, the WPSH and SAH in the AY become weaker and relocate farther north. In addition, the geopotential differences to the north of 50°N are negative, and the minimum is located at around 300 hPa. Accordingly, the positive and negative vertical velocity differences alternate from the equator to the high latitudes, exhibiting a meridional wave train-like pattern between the AY and IY (Figure 11b). This pattern suggests that the abnormal descending (ascending) motions intensified around 30°N (15°N), resulting in less (more) precipitation in the LMYRV (Southern China) in the AY.

Figure 12 presents the tracks of TCs during the simulation period from observations and from the CR simulation. The detection and tracking methods for TC in the CR simulation are the same as those proposed by Kim et al. (2015). The observations included 108 TCs, and the CR included 103 TCs. In both the observations and the CR, most of the TCs formed over the ocean east to the Philippines. After the TCs formed, they tended to move northwestward and then turn northward. In the observations, 33 TCs made landfall on the continent of Asia, and 75 TCs moved to middle and high latitudes. In the CR, the corresponding numbers were 31 and 72. Thus, the CR simulation showed that the WRF could reproduce the tracks of TCs well in the WNP during the integration period. In addition, the TC vortex could not be found in hourly outputs of the SR simulation, which means that the TC did not exist in the SR simulation.

Figure 13 presents the distributions of mean wind fields and geopotential heights averaged over the simulation period at 500 hPa for the observations, CR, and SR, as well as differences between the CR and SR. A comparison of Figure 13a and 13b shows that the CR could simulate the geopotential height and wind vectors well and that the observed and simulated WPSH were almost identical, with the ridgeline at approximately 28°N. The CR-simu-

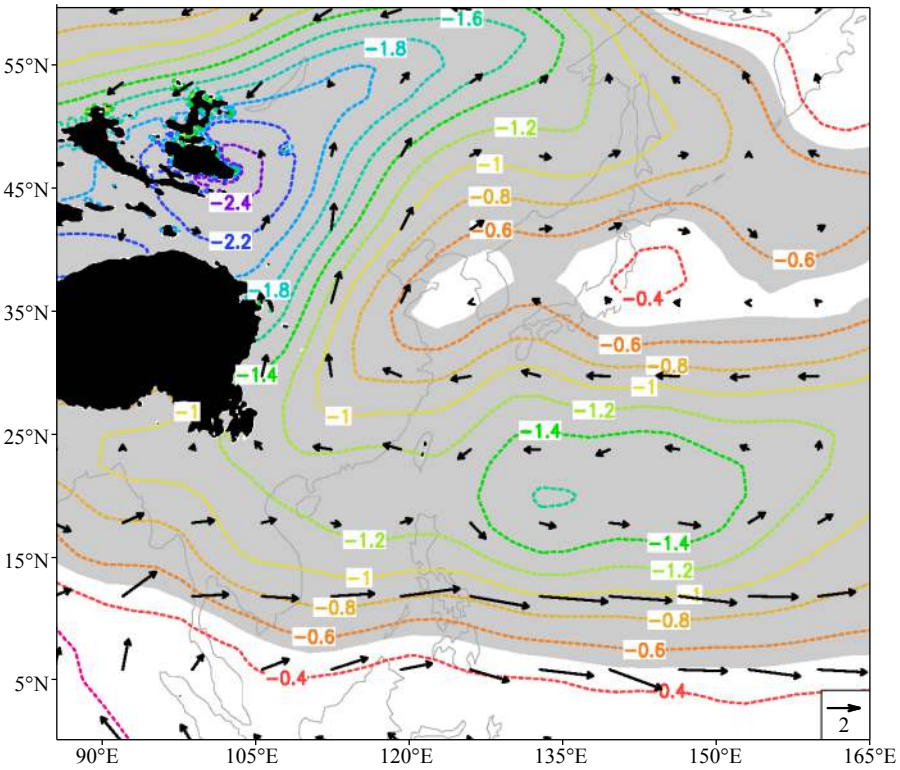

Figure 10. Composite differences in the mean wind field (vectors, units: m·s^{-1}) and geopotential height (solid lines, units: dagpm) averaged from June to August between the AY and IY at 850 hPa. The black-shaded areas indicate a topographic contour of 1,500 m. The gray-shaded areas represent significance at the 95% confidence level or higher for geopotential height.

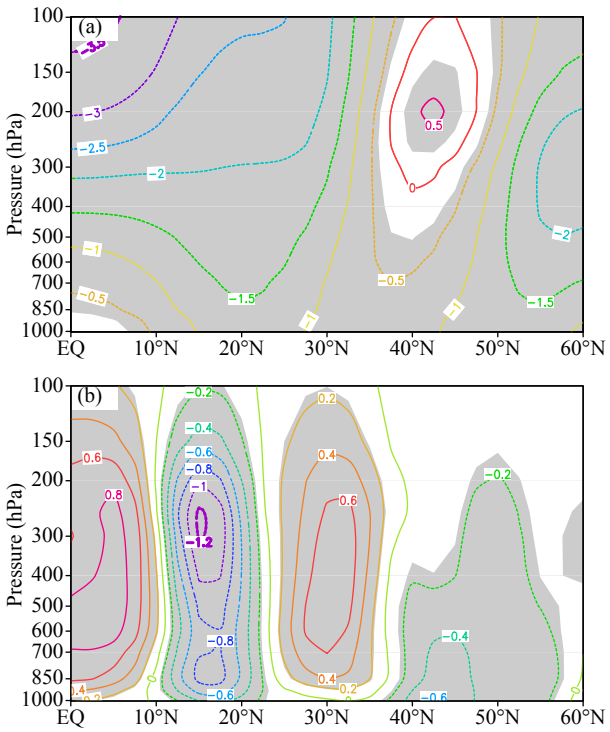

Figure 11. Height–latitude cross sections of differences in the (a) geopotential height (units: dagpm) and (b) vertical velocity (unit: 10^{-4} hPa·s^{-1}) between the AY and IY averaged from June to August and 110°E–150°E. The gray-shaded areas in (a) and (b) represent significance at the 95% confidence level or higher.

lated isohypse of 588 dagpm is mainly located above the ocean to the east of Japan and the East China Sea (Figure 13b). For the SR, the simulated isohypse of 588 dagpm extends to the west of 105°E (Figure 13c). The WPSH is one of the dominant components in the EASM system and is closely related to other components of the EASM system (Lu RY, 2004; Lu RY et al., 2008). It plays an important role in EASM rainfall variation (Ren XJ et al., 2013; Zhang Q et al., 2017). In addition, differences in circulation between the CR and SR exhibit two cyclonic circulations, with the center located over the Bering Sea (50°N, 170°E) and over the sea east to China (40°N, 120°E), respectively (Figure 13d). This result suggests that the TC activities over the WNP can affect circulation far from their tracks by triggering quasi-stationary Rossby waves (Kawamura and Ogasawara, 2006). Moreover, the abnormal quasi-zonal westerlies between the AY and IY cover the region from the equator to about 15°N between 100°E and 150°E, which is similar to the region shown in Figure 10. These sensitivity simulation results indicate that the synoptic TC activities could indeed have great impacts on the large-scale EASM system through dynamic and thermodynamic processes, such as changing the large-scale meridional air temperature gradient by latent heat release (Chen X et al., 2017), heating the upper troposphere by a condensation process in the upper-level outflow of anvil clouds, and cooling the lower troposphere by the evaporation of microphysical particles falling below the 0°C level (Sun Y et al., 2014, 2015), as well as amplifying the upper-level Rossby wave pattern in midlatitude overall as a result of the negative potential vorticity advection by the diabatically driven TC outflows (Archambault et al., 2015; Grams and

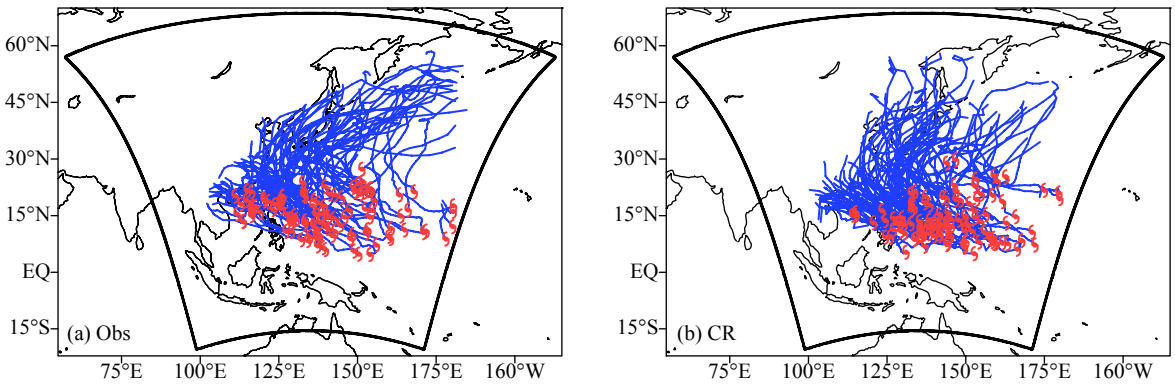

Figure 12. (a) Observed and (b) CR-simulated TC tracks over the simulation period.

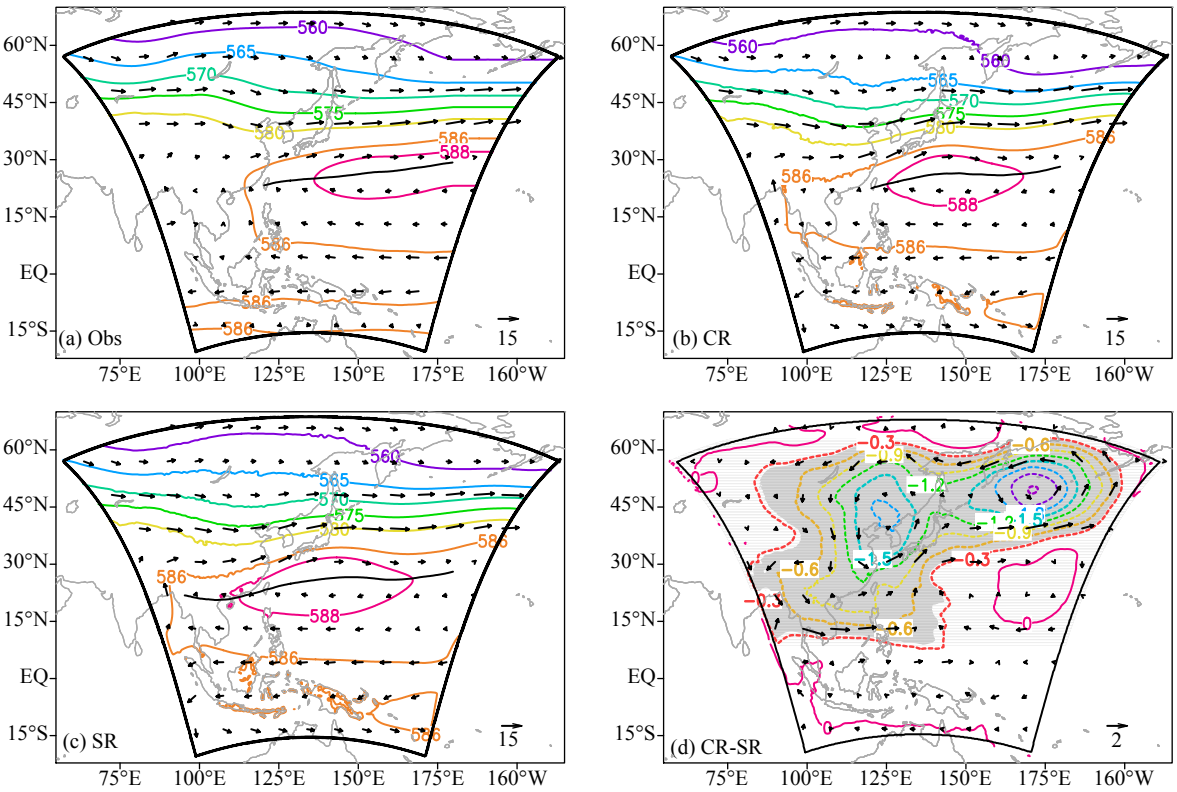

Figure 13. Distributions of the mean wind field (vectors, units: m·s^{-1}) and geopotential height (solid lines, units: dagpm) averaged over the simulation period at 500 hPa for (a) observations, (b) CR, (c) SR, and (d) differences between CR and SR, where the thick solid lines in (a), (b), and (c) indicate the WPSH ridgeline. The gray-shaded areas in (d) represent significance at the 95% confidence level or higher for geopotential height.

Archambault, 2016).

5. Conclusions and Discussion

The present study revealed that the onset of the EASM was earlier with a stronger intensity in the AY than in the IY, and all the major components of the EASM system associated with frequent WNP TC activities were located farther north in the AY relative to those in the IY. Specifically, the southerly monsoon flow in EA could reach higher latitudes in the AY than in the IY. Correspondingly, the EASM rain belt could also shift farther north in the AY and remain in the LMYRV for a relatively short period in the AY, leading to less precipitation there. Likewise, the large-scale atmospheric circulation in the middle and upper troposphere in the AY was significantly different from that in the IY. At 500 hPa, the WPSH was located farther north and east with a weaker intensity in the AY. At 200 hPa, the EASJ axis and the ridgeline of the SAH exhibited a northward displacement, whereas the intensity of the SAH weakened and the position of the SAH moved westward in the AY.

It is well known that the WNP TC activities are controlled by many factors, such as the modulation of the El Niño–Southern Oscillation with large interannual variability (Chan, 2000; Chen TC et al., 2006; Ha Y et al., 2013). The daily frequency of TC occurrence over the WNP from June to August in the AY was always found to be greater than that in the IY. Consequently, cyclonic circulation anomalies in the tropics and anticyclonic circulation in the subtrop-

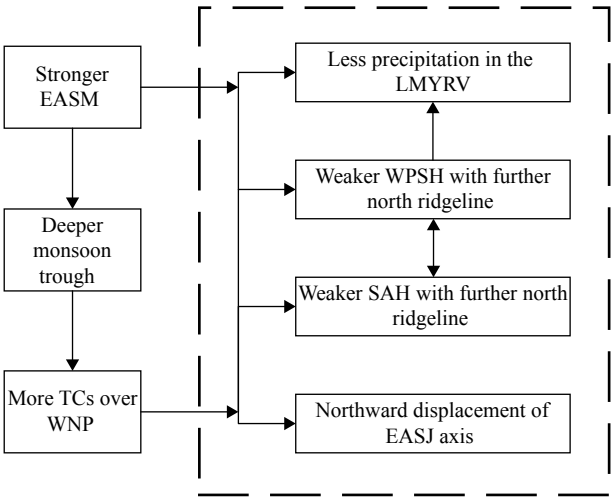

Figure 14. Schematic diagram showing the role of TC activities over the WNP in the EASM system.

ics intensified because of the enhanced Pacific–Japan teleconnection pattern wave trains induced by TC activities over the WNP in the AY. Moreover, the synoptic TC activity would directly affect the large-scale EASM through thermodynamic processes.

On the other hand, a stronger EASM would lead to a deeper monsoon trough in the WNP, which is often accompanied by low-level convergence, cyclonic relative vorticity, small vertical wind shear, a sufficient moisture supply, and high-level divergence. All these conditions are favorable for TC genesis over the monsoon trough (Chen TC et al., 2004). The correlation coefficient between the EASM index and the WNP TC frequency from 1961 to 2010 was estimated at 0.53, which surpassed the 99% confidence level. This result indicates that the intensity of the EASM and the frequency of WNP TC genesis are positively correlated (Choi et al. 2016). As pointed out by Zhang QY and Tao SY (1998), rainfall over the LMYRV decreases when convection in the EA tropical monsoon trough strengthens. Yang H et al. (2011) also found that rainfall in the LMYRV in stronger EASM years was less than that in normal EASM years. Therefore, the stronger EASM itself and the TCs could make similar contributions to the intensity and position of EASM components, as summarized in Figure 14.

Acknowledgments

This work was sponsored by the National Natural Science Foundation of China (41430426, 41805043, 41675077) and the R & D Special Fund for Public Welfare Industry (Meteorology) (GYHY201306025).

References

Archambault, H. M., Keyser, D., Bosart, L. F., Davis, C. A., and Cordeira, J. M. (2015). A composite perspective of the extratropical flow response to recurving western north Pacific tropical cyclones. *Mon. Wea. Rev.*, *143*(4), 1122–1141. https://doi.org/10.1175/MWR-D-14-00270.1

Chan, J. C. L. (2000). Tropical cyclone activity over the western North Pacific associated with El Niño and La Niña events. *J. Climate*, *13*(16), 2960–2972. https://doi.org/10.1175/1520-0442(2000)013<2960:TCAOTW>2.0.CO;2

Chen, T. C., Wang, S. Y., Yen, M. C., and Gallus, W. A. (2004). Role of the monsoon gyre in the interannual variation of tropical cyclone formation over the western North Pacific. *Wea. Forecasting*, *19*(4), 776–785. https://doi.org/10.1175/1520-0434(2004)019<0776:ROTMGI>2.0.CO;2

Chen, T.-C., Wang, S.-Y., and Yen, M.-C. (2006). Interannual variation of the tropical cyclone activity over the western North Pacific. *J. Climate*, *19*(21), 5709–5720. https://doi.org/10.1175/JCLI3934.1

Chen, X., Zhong, Z., and Lu, W. (2017). Association of the poleward shift of East Asian subtropical upper-level jet with frequent tropical cyclone activities over the western North Pacific in summer. *J. Climate*, *30*(14), 5597–5603. https://doi.org/10.1175/JCLI-D-16-0334.1

Choi, K.-S., Cha, Y.-M., Kim, H.-D., and Kang, S.-D. (2016). Possible relationship between East Asian summer monsoon and western North Pacific tropical cyclone genesis frequency. *Theor. Appl. Climatol.*, *124*(1–2), 81–90. https://doi.org/10.1007/s00704-015-1383-4

Fu, B., Peng, S. M., Li, T., and Stevens, D. E. (2012). Developing versus nondeveloping disturbances for tropical cyclone formation. Part Ⅱ: western North Pacific. *Mon. Wea. Rev.*, *140*(4), 1067–1080. https://doi.org/10.1175/2011MWR3618.1

Ge, X. Y., Li, T., and Peng, M. S. (2013). Tropical cyclone genesis efficiency: mid-level versus bottom vortex. *J. Trop. Meteor.*, *19*(3), 197–213.

Grams, C. M., and Archambault, H. M. (2016). The key role of diabatic outflow in amplifying the midlatitude flow: a representative case study of weather systems surrounding western north Pacific extratropical transition. *Mon. Wea. Rev.*, *144*(10), 3847–3869. https://doi.org/10.1175/MWR-D-15-0419.1

Ha, Y., Zhong, Z., Hu, Y. J., and Yang, X.-Q. (2013). Influences of ENSO on Western North Pacific tropical cyclone kinetic energy and its meridional transport. *J. Climate*, *26*(1), 322–332. https://doi.org/10.1175/JCLI-D-11-00543.1

Hsu, H.-H., Hung, C. H., Lo, A.-K., Wu, C.-C., and Hung, C. W. (2008). Influence of tropical cyclones on the estimation of climate variability in the tropical Western North Pacific. *J. Climate*, *21*(12), 2960–2975. https://doi.org/10.1175/2007JCLI1847.1

Hu, C. D., Zhang, C. Y., Yang, S., and Chen, D. K. (2018). Variable correspondence between western North Pacific tropical cyclone frequency and East Asian subtropical jet stream during boreal summer: A tropical Pacific sea surface temperature perspective. *Int. J. Climatol.*, *39*(3), 1768–1776. https://doi.org/10.1002/joc.5905

Huang, G., Qu, X., and Hu, K. M. (2011). The impact of the tropical Indian Ocean on South Asian High in boreal summer. *Adv. Atmos. Sci.*, *28*(2), 421–432. https://doi.org/10.1007/s00376-010-9224-y

Huang, R. H., Chen, J. L., and Huang, G. (2007). Characteristics and variations of the East Asian monsoon system and its impacts on climate disasters in China. *Adv. Atmos. Sci.*, *24*(6), 993–1023. https://doi.org/10.1007/s00376-007-0993-x

Jansen, M., and Ferrari, R. (2009). Impact of the latitudinal distribution of tropical cyclones on ocean heat transport. *Geophys. Res. Lett.*, *36*(6), L06604. https://doi.org/10.1029/2008GL036796

JMA. (2012). Regional Specialized Meteorological Center of Japan Meteorological Agency TC Best Track Data site. Accessed 1 July 2013. Available online at http://www.jma.go.jp/jma/jma-eng/jma-center/rsmc-hp-pub-eg/RSMC_HP.htm

Kalnay, E., Kanamitsu, M., Kistler, R., Collins, W., Deaven, D., Gandin, L., Iredell, M., Saha, S., White, G., … Joseph, D. (1996). The NCEP/NCAR 40-Year reanalysis project. *Bull. Amer. Meteor. Soc.*, *77*(3), 437–472. https://doi.org/10.1175/1520-0477(1996)077<0437:TNYRP>2.0.CO;2

Kawamura, R., and Ogasawara, T. (2006). On the role of typhoons in generating PJ teleconnection patterns over the Western North Pacific in Late Summer. *Sci. Online Lett. Atmos.*, *2*, 37–40. https://doi.org/10.2151/sola.2006-010

Kim, D., Jin, C.-S., Ho, C.-H., Kim, J., and Kim, J. H. (2015). Climatological features of WRF-simulated tropical cyclones over the western North Pacific. *Climate Dyn.*, *44*(11–12), 3223–3235. https://doi.org/10.1007/s00382-014-2410-3

Liao, Z. J., and Zhang, Y. C. (2013). Concurrent variation between the East Asian subtropical jet and polar front jet during persistent snowstorm period in 2008 winter over southern China. *J. Geophys. Res. Atmos.*, *118*(12), 6360–6373. https://doi.org/10.1002/jgrd.50558

Liu, B. Q., Wu, G. X., and Ren, R. C. (2015). Influences of ENSO on the vertical coupling of atmospheric circulation during the onset of South Asian

summer monsoon. *Climate Dyn.*, *45*(7–8), 1859–1875. https://doi.org/10.1007/s00382-014-2439-3

Liu, J., Kuang, X. Y., and Zhang, Y. C. (2010). Relationship between the East Asia subtropical westerly jet in the upper troposphere and the subtropical south Asian high. *Sci. Meteor. Sin.* , *30*(1), 34–41.

Liu, Y. M., and Wu, G. X. (2004). Progress in the study on the formation of the summertime subtropical anticyclone. *Adv. Atmos. Sci.*, *21*(3), 322–342. https://doi.org/10.1007/BF02915562

Lu, R. Y. (2004). Associations among the components of the East Asian summer monsoon system in the meridional direction. *J. Meteor. Soc. Japan*, *82*(1), 155–165. https://doi.org/10.2151/jmsj.82.155

Lu, R. Y., Li, Y., and Ryu, C.-S. (2008). Relationship between the zonal displacement of the western Pacific subtropical high and the dominant modes of low-tropospheric circulation in summer. *Prog. Nat. Sci.*, *18*(2), 161–165. https://doi.org/10.1016/j.pnsc.2007.07.009

Lu, R. Y., Ye, H., and Jhun, J. G. (2011). Weakening of interannual variability in the summer East Asian upper-tropospheric westerly jet since the mid-1990s. *Adv. Atmos. Sci.*, *28*(6), 1246–1258. https://doi.org/10.1007/s00376-011-0222-5

Matsuura, T., Yumoto, M., and Iizuka, S. (2003). A mechanism of interdecadal variability of tropical cyclone activity over the western North Pacific. *Climate Dyn.*, *21*(2), 105–117. https://doi.org/10.1007/s00382-003-0327-3

Qu, X., and Huang, G. (2012). Impacts of tropical Indian Ocean SST on the meridional displacement of East Asian jet in boreal summer. *Int. J. Climatol.*, *32*(13), 2073–2080. https://doi.org/10.1002/joc.2378

Ren, X. J., Yang, X.-Q., and Sun, X. G. (2013). Zonal oscillation of western Pacific subtropical high and subseasonal SST variations during Yangtze persistent heavy rainfall events. *J. Climate*, *26*(22), 8929–8946. https://doi.org/10.1175/JCLI-D-12-00861.1

Ren, X. J., Yang, D. J., and Yang, X.-Q. (2015). Characteristics and mechanisms of the subseasonal eastward extension of the South Asian High. *J. Climate*, *28*(17), 6799–6822. https://doi.org/10.1175/JCLI-D-14-00682.1

Sampe, T., and Xie, S. P. (2010). Large-scale dynamics of the Meiyu-Baiu rainband: environmental forcing by the westerly jet. *J. Climate*, *23*(1), 113–134. https://doi.org/10.1175/2009JCLI3128.1

Skamarock, W. C., Klemp, J. B., Dudhia, J., Gill, D. O., Barker, D. M., Duda, M. G., Huang, X. Y., Wang, W., and Powers, J. G. (2008). A description of the advanced research WRF version 3. NCAR Technical Note NCAR/TN-475+STR. Boulder, Colorado, USA: National Center for Atmospheric Research. https://doi.org/10.5065/D68S4MVH

Su, Z. Z., Yu, J. H., Sun, C. H., Ren, F. M., Wang, Y. Q., and Liang, X. Y. (2010). The initial evaluation of tropical cyclone potential predictability in the Northwestern Pacific using the IPRC regional climate model. *J. Trop. Meteor.* , *26*(2), 165–173. https://doi.org/10.3969/j.issn.1004-4965.2010.02.005

Sun, X. G., Greatbatch, R. J., Park, W., and Latif, M. (2010). Two major modes of variability of the East Asian summer monsoon. *Quart. J. Roy. Meteor. Soc.*, *136*(649), 829–841. https://doi.org/10.1002/qj.635

Sun, Y., Zhong, Z., Lu, W., and Hu, Y. J. (2014). Why are tropical cyclone tracks over the western North Pacific sensitive to the cumulus parameterization scheme in regional climate modeling? A case study for Megi (2010). *Mon. Wea. Rev.*, *142*(2), 1240–1249. https://doi.org/10.1175/MWR-D-13-00232.1

Sun, Y., Zhong, Z., Dong, H., Shi, J., and Hu, Y. J. (2015). Sensitivity of tropical cyclone track simulation over the western North Pacific to different heating/drying rates in the Betts-Miller-Janjić scheme. *Mon. Wea. Rev.*, *143*(9), 3478–3494. https://doi.org/10.1175/MWR-D-14-00340.1

Tao, S. Y., and Chen, L. X. (1987). A review of recent research on the East Asian summer monsoon in China. In C. P. Chang, and T. N. Krishnamurti (Eds.), *Monsoon Meteorology* (pp. 60–92). Oxford: Oxford University Press.

Wang, B., Ho, L., Zhang, Y. S., and Lu, M.-M. (2004). Definition of South China Sea monsoon onset and commencement of the East Asia summer Monsoon. *J. Climate*, *17*(4), 699–710. https://doi.org/10.1175/2932.1

Wang, Z. Q., Duan, A. M., and Wu, G. X. (2014). Time-lagged impact of spring sensible heat over the Tibetan Plateau on the summer rainfall anomaly in East China: case studies using the WRF model. *Climate Dyn.*, *42*(11–12), 2885–2898. https://doi.org/10.1007/s00382-013-1800-2

Yang, H., Zhi, X. F., Gao, J., and Liu, Y. (2011). Variation of East Asian summer monsoon and its relationship with precipitation of China in recent 111 years. *Agric. Sci. Technol.*, *12*(11), 1711–1716. https://doi.org/10.16175/j.cnki.1009-4229.2011.11.012

Yang, J., Bao, Q., Wang, B., Gong, D.-Y., He, H. Z., and Gao, M. N. (2014). Distinct quasi-biweekly features of the subtropical East Asian monsoon during early and late summers. *Climate Dyn.*, *42*(5–6), 1469–1486. https://doi.org/10.1007/s00382-013-1728-6

Zhang, P. F., Liu, Y. M., and He, B. (2016). Impact of East Asian summer monsoon heating on the interannual variation of the South Asian High. *J. Climate*, *29*(1), 159–173. https://doi.org/10.1175/JCLI-D-15-0118.1

Zhang, Q., Zheng, Y. J., Singh, V. P., Luo, M., and Xie, Z. H. (2017). Summer extreme precipitation in eastern China: Mechanisms and impacts. *J. Geophys. Res. Atmos.*, *122*(5), 2766–2778. https://doi.org/10.1002/2016JD025913

Zhang, Q. Y., and Tao, S. Y. (1998). Tropical and subtropical monsoon over East Asia and its influence on the rainfall over eastern China in summer. *Quart. J. Appl. Meteor.* , *9*(S1), 17–23.

Zhong, Z., Tang, X. Z., Lu, W., and Chen, Z. Y. (2015). The relationship of summertime upper level jet over East Asia and the Pacific-Japan teleconnection. *J. Meteor. Sci.*, *35*(6), 672–683. https://doi.org/10.3969/2015jms.0051

Zhu, Z., Zhong, Z., and Ha, Y. (2017). Relationship between typhoon cyclone during Meiyu period over the Northwest Pacific and Jiang-huai Meiyu. *J. Meteor. Sci.* , *37*(4), 522–528. https://doi.org/10.3969/2016jms.0060